nature communications

Article

https://doi.org/10.1038/s41467-025-63089-8

Catalytic cooperation between Ru and Pd atoms on hierarchical porous Ce-based oxide for boosting engine exhaust purification

Received: 1 February 2025

Accepted: 8 August 2025

Published online: 21 August 2025

Check for updates

Linsheng Xu[1], Tian Qin[2], Yuanfeng Li[1], Hao Guo[1], Qiao Hu[2], Jing Xiong[1], Yaxiao Ma[1], Peng Zhang[1], Xiaolin Yu[3] ✉, Xi Liu[2,4], Yunpeng Liu[5,6] ✉, Zhen Zhao[1], Jianping Zou[7] & Yuechang Wei[1] ✉

Simultaneous oxidation of soot and CH_4 emitted from natural gas-diesel dual fuel engine is a new challenge. Herein, a robust catalyst of binary Ru-Pd components supported on three-dimensional ordered macro-mesoporous cerium-zirconium oxide (RuPd/3DOMM-CZO) is elaborately constructed. Ordered macro-mesopore structure in novel hierarchical porous cerium-zirconium oxide can respectively enhance mass transfer of soot and gaseous reactants, and binary Ru-Pd active components can improve activation for NO and CH_4. RuPd/3DOMM-CZO catalyst exhibits excellent catalytic performance and stability during simultaneous soot and CH_4 oxidation. Based on the results of characterizations and theoretical calculations, Ru site in binary Ru-Pd components is responsible for catalyzing NO oxidation to NO_2, which is key step of NO_x-assisted soot oxidation mechanism, while Pd site can activate the C-H bond of CH_4 for boosting oxidation to CO_2; the catalytic cooperation between Ru and Pd atoms can promote the rate-determining step to realize simultaneous oxidation of soot and CH_4.

The natural gas-diesel (dual-fuel) engine with high energy efficiency is an innovative power source for motor vehicles and vessels, but it results in a new challenge to engine exhaust purification[1]. Under the operating conditions of natural gas and diesel fuel, methane (CH_4) and particulate matter (soot), as the important atmospheric pollutants, are simultaneously present in engine exhaust[2]. The catalytic after-treatment technology is an indispensable part for engine exhaust purification[3]. Nowadays, some high-efficient catalysts for single soot or CH_4 oxidation have been reported[4–7]. However, there is a research gap on simultaneous oxidation of soot and CH_4 emitted from dual-fuel engine. Thus, it is urgent and challenging to design and construct the efficient catalysts for boosting purification of engine exhaust.

The catalytic simultaneous oxidation of soot and CH_4 is a typical heterogeneous deep oxidation reaction, which involves a solid catalyst, a solid reactant (soot) and multiple gaseous reactants (O_2, CH_4, and NO)[8]. It is well known that the catalytic performance in heterogeneous oxidation reaction is strongly dominated by two factors: diffusion/mass transfer efficiency of reactants and adsorption/activation properties for reactants[9–12]. It has been found that the mass transfer efficiency of reactants is dependent on the porous nanostructure of the catalyst[13]. The three-dimensional ordered macroporous (3DOM) structure of the catalysts can permit soot particles into the inner space of catalyst with the flow of exhaust gases for improving soot-catalyst contact efficiency[9]. And, the further constructed two-dimensional

[1]State Key Laboratory of Heavy Oil Processing, Key Laboratory of Optical Detection Technology for Oil and Gas, China University of Petroleum, Beijing, China. [2]School of Chemistry and Chemical, In-situ Center for Physical Sciences, Shanghai Jiao Tong University, Shanghai, China. [3]School of Energy and Environmental Engineering, University of Science and Technology Beijing, Beijing, China. [4]School of Chemistry and Chemical Engineering, Ningxia University, Yinchuan, China. [5]Multi-discipline Research Center, Institute of High Energy Physics, Chinese Academy of Sciences, Beijing, China. [6]University of Chinese Academy of Sciences, Chinese Academy of Sciences, Beijing, China. [7]Key Laboratory of Jiangxi Province for Persistent Pollutants Control and Resources Recycle, Nanchang Hangkong University, Nanchang, China. ✉e-mail: yuxl@ustb.edu.cn; liuyunpeng@ihep.ac.cn; weiyc@cup.edu.cn

ordered mesopores on the macroporous wall can reduce the resistance of diffusion/mass transfer of gas molecule, which can facilitate the oxidation of gaseous reactants and the migration of the products (CO_2 and NO_2)[14]. The NO_2 intermediate species, as a powerful oxidant, can boost soot oxidation by the NO_2-assisted catalytic pathway[9,15]. Thus, the design of hierarchical porous material with macroporous and mesoporous structure is a practical approach to enhance diffusion/mass transfer efficiency of reactants during simultaneous oxidation of soot and CH_4.

The adsorption/activation properties of catalysts for reactants are critically related to the stable presence of isolated active sites, which enables simultaneous adsorption/activation of NO and CH_4. Ruthenium (Ru)-based catalysts have been recognized as a promising catalyst for soot oxidation owing to excellent NO adsorption/activation properties[15]. However, the study on the C-H bond activation by Ru site during CH_4 oxidation is lacking, and the thermal stability of Ru at high temperature is still an obstacle to its practical application[16]. Thus, the development of high-efficient and stabilized Ru-based catalysts for soot and CH_4 oxidation is of innovative significance. The micro-modification of Ru active sites can be achieved by adding another platinum group metal for forming a binary Ru-M catalyst[17,18]. Presently, palladium (Pd) is one of the most active elements in realizing catalytic oxidation of CH_4[19,20]. It is a potential strategy to design new binary Ru-Pd catalysts, which can endow Ru-Pd synergistic site for simultaneous activation ability of C-H and N-O bonds, and the thermal stability of Ru component can be also improved by Ru-Pd metal bond.

Herein, we have elaborately fabricated the multifunctional catalysts of binary Ru-Pd active components supported on the surface of $Ce_{0.3}Zr_{0.7}O_2$ with three-dimensional ordered macro-mesoporous structure (RuPd/3DOMM-CZO) via the gas bubbling-assisted membrane reduction (GBMR) method[21]. The hierarchical porous structure can improve the contact efficiency between catalysts and reactants (soot, NO, CH_4, and O_2), and binary Ru-Pd active components have super activation capacity for gaseous reactants. RuPd/3DOMM-CZO catalyst shows excellent catalytic activity and stability for simultaneous oxidation of soot and CH_4. Based on the results of the characterizations and density functional theory (DFT) calculations, it is revealed that the catalytic cooperation between Ru and Pd atoms can promote the oxidation of NO to NO_2, and boost the activation of first C-H bond in CH_4 to realize simultaneous oxidation of soot and CH_4. This study provides a reliable solution for the design of multifunctional catalysts and new insights into the simultaneous oxidation of multiple pollutions emitted from engine exhaust.

Results

Morphology and phase structure of hierarchical porous catalysts

The binary Ru-Pd active components were supported on the inner wall of 3DOMM-CZO support (Fig. S1) by the GBMR method, denoted as RuPd/3DOMM-CZO. The synthesis scheme of RuPd/3DOMM-CZO catalyst is illustrated in Fig. S2. Fig. 1a is the scanning electron microscopy (SEM) image of RuPd/3DOMM-CZO catalyst. It is observed that, after the introduction of binary Ru-Pd active components, the macroporous structure of catalyst is intact, which is derived from the long-range replication of polymethyl methacrylate (PMMA) microspheres templates (Fig. S3), indicating the well-qualified mechanical stability of 3DOMM-CZO support.

To visualize the existence of hierarchical porous structure with macropore and mesopore, the annular dark-field scanning transmission electron microscopy (ADF-STEM) images of RuPd/3DOMM-CZO catalyst are shown in Fig. 1b, c. As shown in Fig. 1b, the catalyst presents the three-dimensional ordered macroporous skeleton with diameter of 250 nm, which is large enough to permit soot particles (10-30 nm particle sizes) into the interior of the catalyst[22]. As shown in Figs. 1c and S4, the ordered mesoporous structure is distributed in the form of 2D hexagonal (P6mm) on the macroporous walls, which is derived from the Pluronic F127 templates. The N_2 adsorption-desorption isotherms of the catalysts (Fig. S5a) have obvious H4 ($P/P_0 = 0.4–0.7$) and H3 ($P/P_0 = 0.8–1.0$) hysteresis loops, suggesting the formation of ordered mesoporous and macroporous structure, respectively.

In high-resolution ADF-STEM image of RuPd/3DOMM-CZO catalyst (Fig. 1d), the interplanar d-spacing of Ce-Zr solid solution is 0.31 nm corresponding to the exposed (111) facet, and the distinct step sites can be observed at the edges of the Ce-Zr oxide. The strain distribution maps of RuPd/3DOMM-CZO catalyst from geometrical phase analysis (GPA) are depicted in Fig. S6. Based on the GPA analysis, the main zone of the catalyst (shown mainly in red) shows a strain value of almost 0%, suggesting that the strain effect is not a major factor influencing the RuPd cooperation[23]. As shown in Fig. S7, RuPd NPs were supported on 3DOMM-CZO with a relatively concentrated particle size of ~7.41 nm. To further observe the microstructure of binary Ru-Pd components, Fig. 1e exhibits the high-resolution bright-field scanning transmission electron microscopy (BF-STEM) image of RuPd/3DOMM-CZO catalyst, the interplanar d-spacing are 0.19 and 0.31 nm, corresponding to the exposed (111) facet of RuPd alloy and (111) facet of Ce-Zr oxide, respectively[24]. Figure 1f shows the high-resolution ADF-STEM image of RuPd/3DOMM-CZO catalyst. One RuPd nanoparticle (NP), with interplanar d-spacing of 0.26 nm corresponding to (101) facet of oxygen-adsorbing RuPd NPs, is located on the surface of Ce-Zr support. It indicates that metal and oxide states of binary Ru-Pd components coexist on the surface of catalyst. The X-ray diffraction (XRD) patterns are shown in Fig. S8. After the introduction of supported Ru and Pd components, the diffraction peaks of (111), (200), and (311) crystal facets slightly shift to left, which may be due to the change in the redox state of the CZO bulk by the Ru/Pd on the surface. The EDX line-scanning analysis of the binary RuPd NP verifies the formation of atomic-level Ru-Pd homogeneous phase (Fig. S9). And the element distribution mapping of RuPd/3DOMM-CZO catalyst further indicates homogeneous dispersion of binary Ru-Pd components on the surface of Ce-Zr solid solution (Fig. S10).

Catalytic performances for simultaneous oxidation of soot and CH_4

The catalytic performances of the catalysts for simultaneous oxidation of soot and CH_4 were investigated by temperature-programmed oxidation (TPO), and the single Ru or Pd catalysts as references are also listed (Fig. 2a, b), and the complete temperature-conversion curves from the beginning to the end of the reaction are shown in Fig. S11. The catalytic activity for simultaneous oxidation of soot and CH_4 is assessed by the T_{10}, T_{50} and T_{90} values, defined as temperatures at 10%, 50%, and 90% conversion of soot and CH_4, respectively (Table S2). Under the conditions of without catalyst, it is very difficult to achieve the simultaneous oxidation of soot and CH_4, whose T_{50} values are respectively 592 and 692 °C. It is higher than the temperature of engine exhaust (<400 °C)[25]. Thus, it is important to design the catalyst for boosting simultaneous oxidation of soot and CH_4 at the exhaust temperature. 3DOMM-CZO catalyst exhibits higher simultaneous oxidation activity of soot (T_{50} = 418 °C) and CH_4 (T_{50} = 620 °C) in comparison with three-dimensional ordered macroporous Ce-Zr oxide (3DOM-CZO) and mesoporous Ce-Zr oxide (Meso-CZO) catalysts (Fig. S12), indicating that the hierarchical porous structure can enhance the catalytic performance for simultaneous oxidation of soot and CH_4.

After the introduction of Ru and/or Pd component, their catalytic activities are remarkly improved, which is attributed to enhance adsorption-activation capacities for gaseous reactants (Fig. 2a, b). The activity of RuPd/3DOMM-CZO catalyst during simultaneous oxidation of soot and CH_4 is strongly dependent on the Ru/Pd ratio in binary RuPd active components (Fig. S13). Among the catalysts, RuPd/

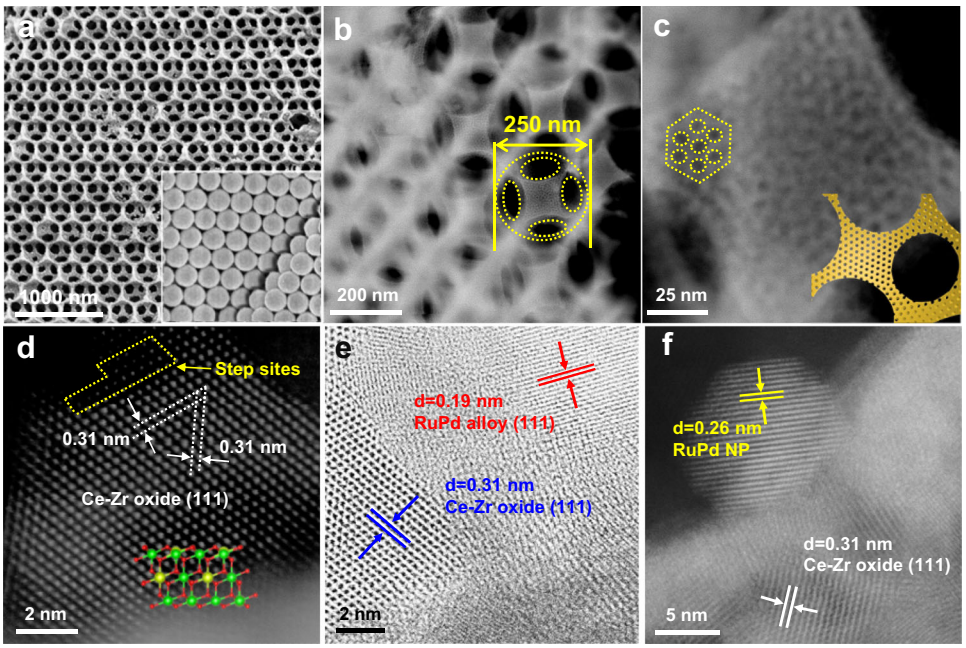

Fig. 1 | Hierarchical pore morphology and microstructure of RuPd/3DOMM-CZO catalyst. SEM (**a**), ADF-STEM images of 3D macroporous skeleton (**b**) and 2D hexagonal (P6mm) mesoporous structure (**c**), high-resolution ADF-STEM (**d**, **f**) and high-resolution BF-STEM (**e**) images of the catalyst. The inset in (**a**) is PMMA template of 3DOMM catalyst. The inset in (**c**) is a model of mesopores on the macroporous walls. The inset in (**d**) is the standard atomic structure of Ce-Zr oxide on (111) orientation. **e**, **f** shows the interface between RuPd NP and 3DOMM-CZO support.

3DOMM-CZO catalyst (the Ru/Pd mass ratio is 1:1) exhibits the best catalytic performances and the binary-metal cooperation-dependence activity during the simultaneous oxidation of soot and CH_4, i.e., its T_{50} values of soot and CH_4 oxidation are 357 and 334 °C, respectively, which is 74 and 212 °C lower than those of single Pd catalyst for soot oxidation and single Ru catalyst for CH_4 oxidation, respectively. And RuPd/3DOMM-CZO catalyst can achieve completely simultaneous oxidation of soot and CH_4 below 410 °C, which is fulfilled by Ru/3DOMM-CZO catalyst at 650 °C (Fig. S14). In addition, the selectivity of soot and CH_4 oxidation to CO_2 product over RuPd/3DOMM-CZO catalyst is above 99% (Fig. S15), indicating that CO pollutant derived from engine exhaust can be immediately removed by the catalyst. To explore the reaction energy barrier on RuPd/3DOMM-CZO catalysts during soot and CH_4 oxidation, the apparent activation energy (E_a) was evaluated under an approximate kinetic regime of the low-temperature range (Fig. S16). The RuPd/3DOMM-CZO catalyst exhibits the lowest apparent activation energy for soot (48.4 kJ mol^{-1}) and CH_4 (63.5 kJ mol^{-1}) oxidation, which is far lower than those of 3DOMM-CZO and single Ru/Pd catalysts, indicating that binary Ru-Pd active components play a pivotal role in catalyzing soot and CH_4 oxidation.

It is well known that nitrogen oxides (NO_x) in engine exhaust is important to catalytic soot oxidation via the NO_x-assisted oxidation mechanism[26]. However, it is still unclear to understand the role of NO_x during simultaneous oxidation of soot and CH_4. To investigate the effect of NO on simultaneous soot and CH_4 oxidation, Fig. 2c shows the conversion curves of CH_4 oxidation over the catalysts at a fixed temperature. In the presence of NO, the conversion rates of CH_4 over Ru-based catalysts significantly decrease compared with that in the absence of NO, while its disturbance over Pd/3DOMM-CZO catalyst can be ignored. It suggests that NO can inhibit CH_4 oxidation over Ru-based catalysts, but not over Pd/3DOMM-CZO catalyst during simultaneous oxidation of soot and CH_4. As shown in Fig. 2d, introducting NO into the reaction atmosphere, the conversion curves of soot oxidation over the catalysts shift to the lower temperature during simultaneous oxidation of soot and CH_4. And the T_{50} value of soot oxidation over three catalysts decreases more than 50 °C. It indicates that the presence of NO can promote the soot oxidation, and the catalytic activity of Ru-based catalysts for soot oxidation is more dependent on the role of NO compared with Pd-based catalysts. As shown in Fig. 2e, the conversion curves of CH_4 oxidation over Ru-based catalysts in the presence of NO shift to the higher temperature during simultaneous oxidation of soot and CH_4. But the T_{50} value of CH_4 oxidation over RuPd/3DOMM-CZO catalyst reduces even less than Ru/3DOMM-CZO catalyst. It suggests that the binary RuPd active structure in RuPd/3DOMM-CZO catalyst can release the disinhibition of NO during CH_4 oxidation. Thus, the reaction of CH_4 oxidation over the catalysts is a competitive reaction to NO oxidation, which is key step of catalytic soot oxidation. And the cooperation between Ru and Pd atoms in binary RuPd active component is an effective strategy to boost simultaneous oxidation of soot and CH_4.

The catalytic and structural stability of RuPd/3DOMM-CZO catalyst is important to practical application. The catalytic stability of RuPd/3DOMM-CZO catalyst was tested by consecutive TPO reactions and hydrothermal aging treatment. As shown in Fig. 2f, g, RuPd/3DOMM-CZO catalyst exhibits good catalytic stability for simultaneous soot and CH_4 oxidation, and its T_{50} values varies within 3 °C during five cycle tests of TPO. As shown in Fig. S17, the simultaneous soot and CH_4 oxidation activities of the RuPd/3DOMM-CZO catalyst after high temperature and high humidity environments remained stable compared to the fresh catalyst. Figure S18 shows the SEM and TEM images of RuPd/3DOMM-CZO catalyst after catalytic stability testing. The hierarchical porous structure of the catalysts keeps perfect, illustrating the excellent structural stability of hierarchical porous catalysts. The stable mechanical structure of Ce-based hierarchical porous catalysts can be attributed to the introduction of Zr into CeO_2 to form a Zr-Ce solid solution. The excellent stability of the catalysts is potential to practical application.

Surface chemistry states and adsorption/activation capacity of catalysts

X-ray photoelectron spectroscopy (*XPS*) was conducted to investigate the surface chemistry states of the catalysts, and the resulsts are shown

https://doi.org/10.1038/s41467-025-63089-8

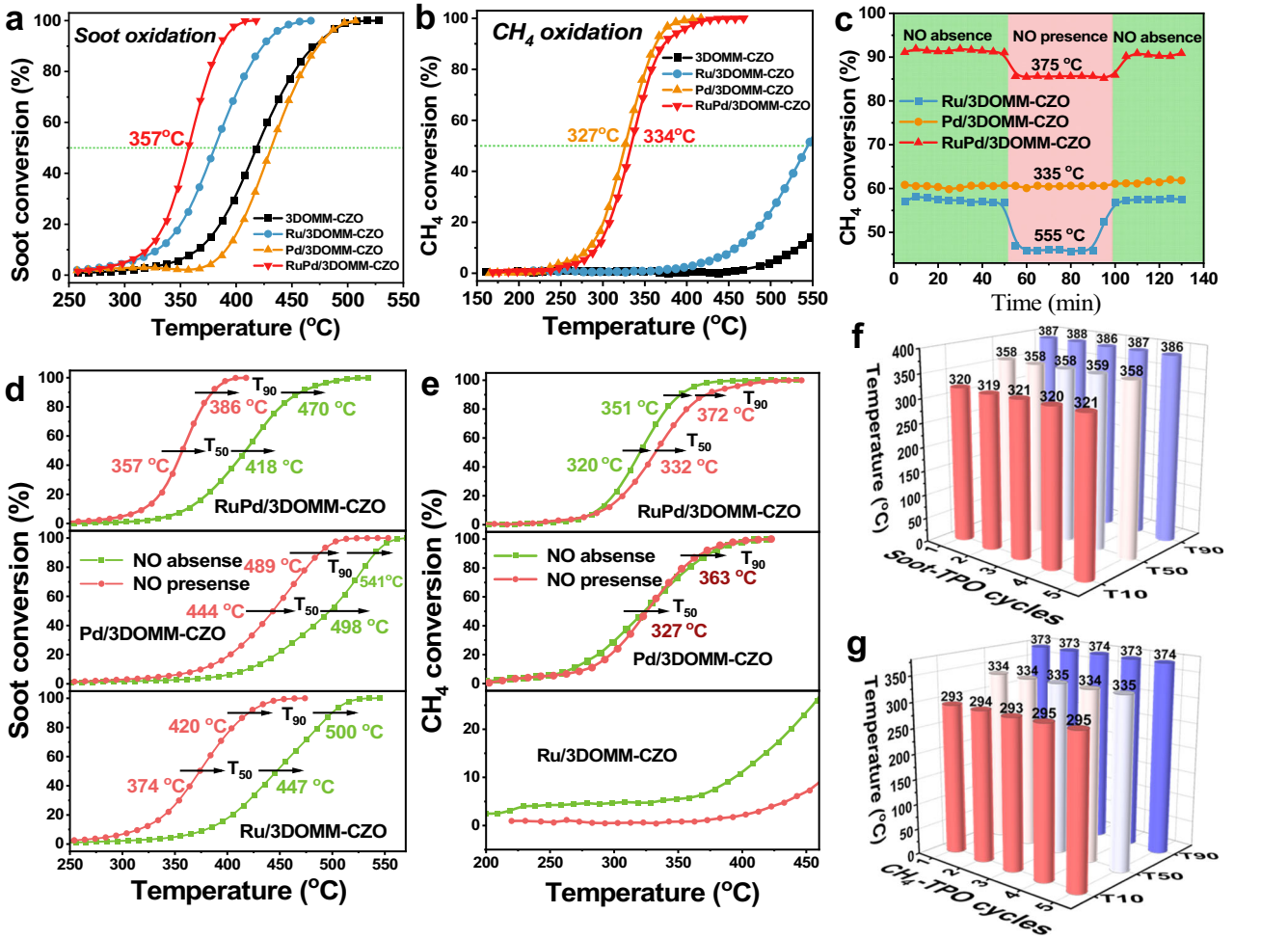

Fig. 2 | Catalytic performances of the catalysts for simultaneous soot and CH_4 oxidation. Temperature-conversion curves of catalytic soot (**a**) and CH_4 (**b**) oxidation. CH_4 conversion at fixed temperature in the presence/absence of NO (**c**). Temperature-conversion curves for simultaneous soot (**d**) and CH_4 (**e**) oxidation in the presence/absence of NO. Stability of RuPd/3DOMM-CZO catalyst after five-cycle tests for simultaneous soot (**f**) and CH_4 (**g**) oxidation.

in Fig. S19 and Table S3. As shown in Fig. S19a, the deconvolved results of Ru *3p* spectra contain two pairs of peaks at 461.6, 483.5 and 464.1, 485.8 eV belonging to the metallic (Ru^0) and oxidized (Ru^{n+}) states, respectively. And the proportion of metallic Ru species (59.7%) in RuPd/3DOMM-CZO catalyst decreases compared with Ru/3DOMM-CZO catalyst (67.5%). Only the Pd $3d_{5/2}$ component was analyzed to avoid effects arising from the overlap of Pd 3d spectrum and Ca *2p* line (or possibly Mg *KLL*). In Fig. S19b, Pd *3d* spectra are deconvoluted to three peaks, which are assigned to Pd^0 (335.1 eV), Pd^{2+} (336.8 eV), Pd^{4+} (339.2 eV) species. The deconvolution results of Pd *3d* show that the proportion of Pd^0 species in RuPd/3DOMM-CZO catalyst increases to 60.5% compared with Pd/3DOMM-CZO catalyst (54.7%). In contrast to single Ru and Pd catalysts, the Ru^{n+}/Ru^0 ratio of RuPd/3DOMM-CZO catalyst increases, while its ratio of $(Pd^{2+}+Pd^{4+})/Pd^0$ decreases. It indicates that the formation of binary RuPd alloy can change the electronic environment of Ru and Pd, resulting in atomic Ru-Pd cooperation. The deconvolved curves of Ce *3d* spectra include 10 or 11 peaks (Fig. S19c), and the peaks located at 882.4, 888.4, 900.8, and 906.6 eV are assigned to Ce^{3+} species, and other peaks are assigned to Ce^{4+} species. The Ce spectrum of 3DOMM-CZO and Ru/3DOMM-CZO catalysts shows the additional peak at ~916 eV contrasting with the standard Ce spectrum. It is attributed to that the existence of structural defects leads to a valence state of Ce between +3 and +4[27]. RuPd/3DOMM-CZO catalyst has the highest Ce^{3+} content (35.8%) in comparison to the single Ru and Pd catalysts. It suggests that the binary Ru-Pd components can induce the surface lattice transformation from Ce^{4+} into Ce^{3+} cations. Furthermore, the increasing Ce^{3+} content can induce the formation of oxygen vacancies on the catalyst surface, which is critical to the increasing of active oxygen species. As shown in Fig. S19d, the O *1s* spectra are deconvoluted into three peaks corresponding to lattice oxygen (O^{2-}) (~529.7 eV), surface peroxide (O_2^{2-}) (~531.3 eV) and super-oxygen (O_2^-) (~532.7 eV). The O_2^{2-} and O_2^- species are considered to active oxygen species for deep oxidation reaction. The $(O_2^- + O_2^{2-})/O^{2-}$ ratio in RuPd/3DOMM-CZO catalyst is the highest (0.45), suggesting that the binary Ru-Pd active components enhance the adsorption-activation of O_2, which is responsible for boosting the simultaneous oxidation of soot and CH_4.

X-ray absorption fine structure (XAFS) spectra of Ce L_3-edge was collected to further investigate the neighbor structure around Ce atoms of catalysts (Fig. 3a)[28,29]. The Ce L_3-edge near-edge XAFS (NEXAFS) spectra of the catalysts can be well fitted by four peaks (A, B, C, and D) using arctangent function and Gaussian function. Peak (A) is attributed to O *2p*-Ce *5d* hybridization, and the formation of (B) peak is related to the Ce^{3+} species[30,31]. The (C) and (D) peaks correspond to the characteristic electron transitions of Ce^{4+} species[32]. The Ce^{3+} concentration in the catalysts can be calculated from the area of (B) peak (Table S4). The Ce^{3+} concentration of RuPd/3DOMM-CZO catalyst is the highest (23.5%), which is consistent with the results of Ce *3d*. It confirms that the unsaturated coordination of Ce^{3+} species is generated on RuPd/3DOMM-CZO catalyst. The information on the

https://doi.org/10.1038/s41467-025-63089-8

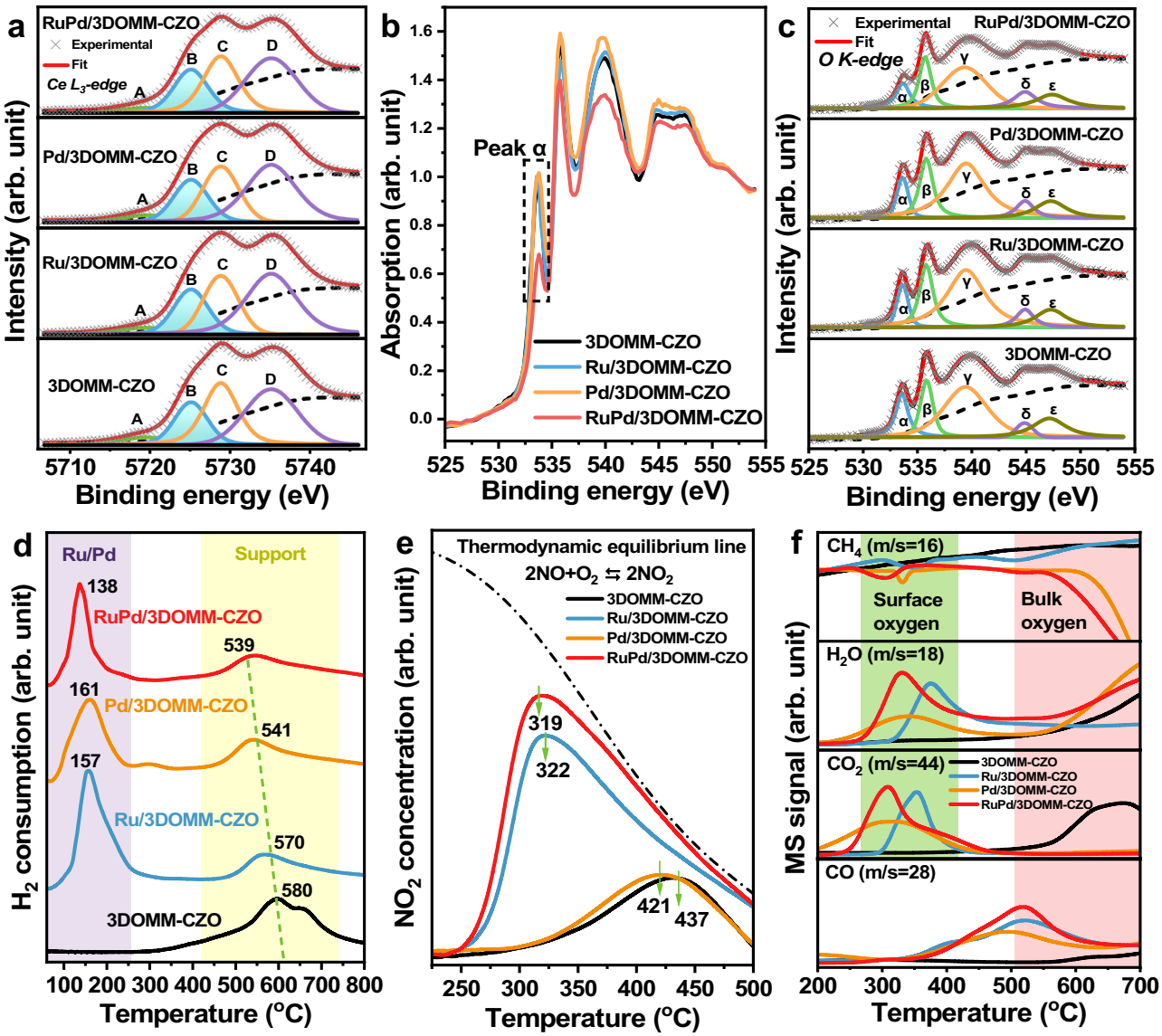

Fig. 3 | The oxygen vacancy density and adsorption-activation capacities of the catalysts for NO, CH_4, and O_2. Ce L_3-edge XAFS spectra fitting results (**a**), O K-edge sXAS spectra (**b**), O K-edge sXAS fitting results (**c**), H_2-TPR (**d**), NO-TPO (**e**), and CH_4-TPSR (**f**) of catalysts.

hybridization between O *2p* and Ce *2p* states is obtained by probing the O *1s*→Ce *2p* transition using the O K-edge soft X-ray absorption spectra (sXAS) (Fig. 3b). In the ground state of Ce-Zr oxides, the O *2p* valence band is filled completely, which hybridizes with the Ce *4f* orbitals aggressively. Thus, it can be observed that the (α) peak is attributed to the transition from the O *1s* to p-symmetry components of Ce *4f* orbitals. As shown in Fig. 3b, the (α) peak of the RuPd/3DOMM-CZO catalyst is significantly smaller, implying the Ce *4f* orbitals are partially filled with electrons forming the Ce^{3+} ($4f^1$) state, while reducing the Ce^{4+} ($4f^0$) state because of the formation of oxygen vacancies. Ru or Pd embedding in Ce-based supports can lead to electron migration from RuPd to the support and defect formation on CZO. The increase in Ce^{3+} content is mainly due to electron migration from RuPd components to 3DOMM-CZO, which leads to Ce^{4+} changing to Ce^{3+}. It is consistent with the analysis results of Ce L_3-edge NEXAFS spectra. Other four peaks labeled as β, γ, δ, and ε also arise in the O K-edge sXAS. The (β) and (γ) peaks are attributed to transition from O *1s*→Ce *5d* (e_g) and O *1s*→Ce *5d* (t_{2g}) levels in the conduction band, respectively. The (δ) and (ε) peaks are also obtained at the higher energy side because of the local hybridization of Ce *4f* and O *2p* state electronic levels.

The concentration of oxygen vacancies in the lattice of Ce-based oxides can be estimated by the area ratio between (β) and (γ) peaks (defined as I_β/I_γ). As shown in Fig. 3c and Table S4, the fitting results of O K-edge over RuPd/3DOMM-CZO catalyst possess the largest I_β/I_γ value, indicating that the binary Ru-Pd components can induce the generation of Ce^{3+} species and oxygen vacancies on Ce-Zr oxides significantly[33]. It results from the strong Ru/Pd-O-Ce electronic interaction, which is crucial for boosting the catalytic activity of deep oxidation. In Raman spectra (Fig. S20), the relative intensity of two peaks, associated with oxygen defect (*D*) and F_{2g} symmetric stretching mode of the oxygen atoms (denoted as I_D/I_{F2g}), are used to assess the surface density of oxygen vacancies. The results obtained by Raman spectra are consistent with that of O K-edge sXAS (Table S4). The O_2 molecule can be adsorbed directly onto the catalyst surface to form superoxide species (O_2^-) species[34]. In addition, oxygen vacancies contribute to the adsorption-activation of O_2 to form active oxygen species, i.e., the O_2 molecule can occupy the oxygen vacancy on Ce-based support forming peroxide (O_2^{2-}) species, which can react with NO and CH_4[35]. In-situ Raman experiments were performed to dynamically examine the density of oxygen vacancies on the RuPd/3DOMM-CZO support during simultaneous NO and CH_4 oxidation. As shown in Fig. S21, after the

introduction of 5% vol O_2 for 10 and 20 min, the I_D/I_{F2g} value was reduced to 1.06 and 0.85, respectively, relative to the conditions in the absence of O_2 (I_D/I_{F2g} = 1.50). It indicates that the oxygen vacancies are gradually filled by O_2 molecules in this process. And the peaks attributed to superoxide (O_2^-) at ~1043 cm^{-1} become stronger progressively with the introduction of O_2, indicating that O_2 is also adsorbed on the catalyst surface. But the peak of peroxide (O_2^{2-}) species at ~847 cm^{-1} is not present in the in-situ Raman spectra clearly, which may be due to the O_2 decomposition. Then, the gas feed was switched to a 0.1 % vol NO/0.1 % vol CH_4 flow. After the introduction of NO/CH_4 for 10 and 20 min, the I_D/I_{F2g} value was increased to 0.99 and 1.33, respectively. It implies that the O_2 adsorbed on the oxygen vacancy is consumed by NO/CH_4 oxidation resulting in elevated oxygen vacancy density.

The redox property is crucial for the catalytic activity during deep oxidation reaction, which can be evaluated by temperature-programmed reduction of H_2 (H_2-TPR), and the result is shown in Fig. 3d. For 3DOMM-CZO support, one peak at 580 °C is related to the reduction of Ce^{4+} to Ce^{3+} species (light yellow region). After the introduction of Ru, Pd and binary Ru-Pd components, the reduction peak of Ce^{4+} to Ce^{3+} species shifts to a relatively low temperature, indicating that the redox property of the catalysts can be improved by the strong metal-support interaction between Ce-Zr oxides and Ru/Pd components. For supported Ru, Pd and RuPd catalysts, one reduction peak at low-temperature region (purple region) can be observed, which is assigned to the reduction of noble metal oxides and the interfacial oxygen (Ru/Pd-O-Ce)[36]. The single Ru and Pd catalysts show two peaks at 157 and 161 °C, which is assigned to reduction of RuO_x and PdO_x species, respectively. RuPd/3DOMM-CZO catalyst exhibits the lowest reduction temperature (138 °C), indicating that the redox capacity of catalysts can be enhanced by Ru-Pd cooperation at atomic scale. The initial H_2 consumption rate (Fig. S22) can reflect the low-temperature surface oxygen species activity of catalysts. The initial H_2 consumption rate for the RuPd/3DOMM-CZO catalyst (0.369 mmol g_{cat}^{-1} s^{-1}) is seven-fold of bare 3DOMM-CZO catalyst (0.052 mmol g_{cat}^{-1} s^{-1}), resulting in low-temperature oxidation of soot and CH_4.

During soot oxidation, active oxygen species on the surface of catalysts can react with NO species to form NO_2 intermediate with strong oxidizing, which promotes soot oxidation to CO_2. Thus, the oxidation efficiency of soot can be improved by oxidizing NO to NO_2 via NO_2-assisted mechanism. The temperature-programmed oxidation of NO (NO-TPO) was applied to evaluate the NO adsorption-activation capacity of catalysts. As shown in Fig. 3e, the single Ru catalyst exhibits a lower temperature of NO_2 concentration peak and a much higher NO_2 concentration compared with the single Pd catalyst, indicating that the Ru active component is primarily responsible for NO oxidation rather than Pd. And the NO_2 concentration peak of RuPd/3DOMM-CZO catalyst has the lowest temperature (319 °C), its intensity is the highest. Thus, the binary Ru-Pd atoms cooperation can enhance adsorption-activation capacity for NO.

The temperature-programmed surface reaction of CH_4 (CH_4-TPSR) experiment was applied to further investigate the adsorption-activation capacities of CH_4 and O_2. As shown in the CH_4-TPSR curve of Fig. 3f, the peak temperature of CH_4 consumption over single Pd catalyst (331 °C) is lower than single Ru catalyst (351 °C), suggesting that the Pd component is critical for adsorption-activation of CH_4 compared to Ru component. And RuPd/3DOMM-CZO catalyst shows the lowest peak temperature of CH_4 consumption (306 °C). Thus, the atomic Ru-Pd cooperation in the catalysts can effectively enhance the consumption capacity for CH_4 via surface oxygen species (green region). The O_2 adsorption-activation capacity of the catalysts can be measured by H_2O and CO_2 signals, which originate from complete oxidation of CH_4 in the presence of sufficient surface oxygen species. RuPd/3DOMM-CZO catalyst exhibits the strongest peak intensity of H_2O and CO_2, reflecting the strongest O_2 adsorption-activation capacity. The great O_2 adsorption-activation capacity of the catalyst is vital for boosting the deep oxidation reaction. The CO is the product of incomplete oxidation of CH_4 depending bulk oxygen in the high-temperature region (pink region). It indicates that, after almost complete depletion of surface oxygen, the bulk oxygen of RuPd/3DOMM-CZO catalyst is potential to realize CH_4 oxidation.

Intermediate Species and Reaction Pathways During Simultaneous Oxidation of Soot and CH_4

To insight into intermediate species of binary Ru-Pd catalysts for simultaneous oxidation of NO and CH_4, Fig. 4 shows the in-situ diffuse reflectance infrared Fourier transform spectra (in-situ DRIFTS) under conditions of reaction atmosphere. As shown in Fig. 4a, d, the peaks in the region of 3500–3800 cm^{-1} are ascribed to the desorption of water or hydroxyl groups[37]. The characteristic peaks of NO oxidation are assigned to bidentate nitrates (1586 cm^{-1}), linear nitrites (1480 cm^{-1}), free ionic nitrates (1378 cm^{-1}), monodentate nitrates (1300 cm^{-1})[38–41]. With the temperature rising, the peak intensity of linear nitrites (1480 cm^{-1}) and monodentate nitrates (1300 cm^{-1}) become weaker gradually. Moreover, the rising temperature also results in the gradual appearance of characteristic peaks of bidentate nitrates (1586 cm^{-1}) and free ionic nitrates (1378 cm^{-1}), and the characteristic intensity of free ionic nitrates increases significantly. It suggests that the adsorbed NO_x species gradually transform into labile NO_3^- intermediates, and subsequently decompose into NO_2.

As shown in Fig. 4b, e, the double peaks in the range of 2280–2400 cm^{-1} are attributed to the stretching vibration of adsorbed CO_2, and its intensity increases with the rise of temperature[42]. The peaks at 1305 and 3013 cm^{-1} are assigned to the bending and strong characteristic antisymmetric stretching signals for free CH_4 molecules, respectively[37]. With the temperature rising, the intensities of peak decreases, suggesting that CH_4 is consumed to produce CO_2. At below 350 °C, the peak at 1467 cm^{-1} can be attributed to the bending of methoxy species (*OCH_3)[43]. And the peak at 1374 cm^{-1} can be ascribed to the formate species (HCOO*) with temperatures above 200 °C[44]. The first C-H bond of the CH_4 molecule is broken to obtain the methyl group (−CH_3), which combines with the oxygen atom on the surface of the catalyst to form the methoxy species. With the temperature rising, the methoxy species continue to dehydrogenate and react with oxygen species to formate species. And, the formate species will decompose into CO_2, eventually[37].

Figure 4c, f depict the process of simultaneous oxidation under conditions of NO (0.1vol %) and CH_4 (0.1vol %), which is a similar evolution of in-situ DRIFTS to the NO oxidation, i.e., those peaks almost coincide the NO oxidation in the range of 1000 to 1600 cm^{-1}. In Fig. 4c, the characteristic peaks of intermediates (formate and methoxy) during CH_4 oxidation are masked by the intermediate peaks of NO oxidation. It demonstrates the competitive oxidation of CH_4 and NO over RuPd/3DOMM-CZO catalyst, where CH_4 oxidation is inhibited by NO. In the process of simultaneous oxidation, the free ionic nitrates exhibit the strongest peak, combined with NO_x adsorption behaviors, thus, the free ionic nitrates are recognized as the key intermediates. And the gaseous reactants (NO and O_2) can be absorbed on the binary Ru-Pd active site and converted to NO_3^- intermediates, which then decompose into NO_2 for boosting soot oxidation.

To further illustrate the role of Ru and Pd active components and the advantages of binary Ru-Pd cooperation during the simultaneous oxidation reaction, the DFT calculations were carried out. We build the structures of Ru/CZO, Pd/CZO and RuPd/CZO catalysts for NO and CH_4 oxidation, and the detailed model is shown in Fig. S23. The path and energy for catalyzing NO oxidation to NO_2 can be divided into the following six stages (Figs. 5a and S24). Firstly, a gaseous NO molecule is adsorbed on the active site of catalysts via O-N-M (M = Ru or Pd) bonds forming surface NO^* species. The NO adsorption energies (E_{ads}(NO)) at Ru/CZO, Pd/CZO and RuPd/CZO catalysts are −2.65, −2.37, and

https://doi.org/10.1038/s41467-025-63089-8

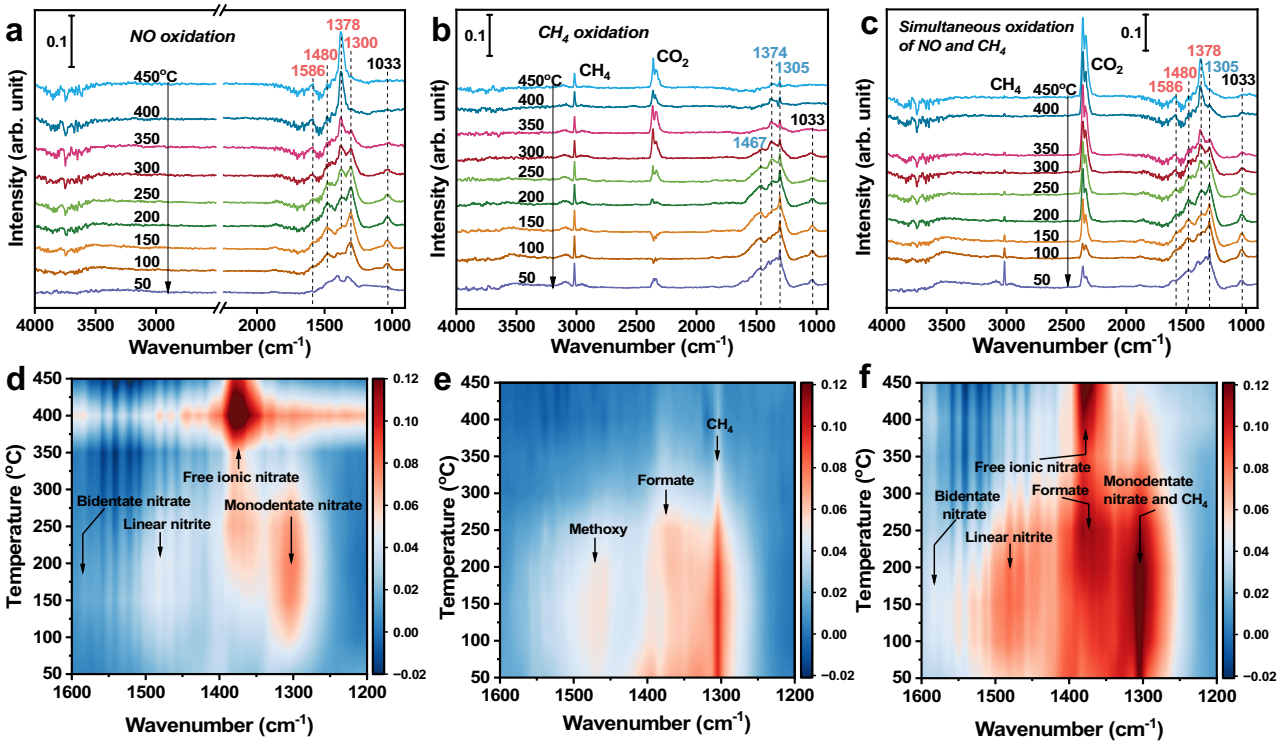

Fig. 4 | Intermediate species and reaction mechanisms in different gas reaction conditions over RuPd/3DOMM-CZO catalyst. Temperature-dependent in-situ DRIFT spectra (**a**) and corresponding contour projection results (**d**) of NO oxidation. Temperature-dependent in-situ DRIFT spectra (**b**) and corresponding contour projection results (**e**) of CH_4 oxidation. Temperature-dependent in-situ DRIFT spectra (**c**) and corresponding contour projection results (**f**) of simultaneous NO and CH_4 oxidation.

−3.21 eV, respectively, indicating that the adsorption of single Ru site for NO is stronger than single Pd site, and the binary RuPd site exhibits the strongest adsorption capacity of NO. Secondly, a gaseous O_2 is adsorbed at the interface between noble metal sites (Ru, Pd, and RuPd) and Ce-Zr support via O-Ce and O-M (M = Ru or Pd) bonds forming surface adsorbed O_2^*. The ensemble of binary RuPd clusters and Ce-Zr solid solutions is responsible for adsorption-activation of O_2. The O_2 adsorption energies ($E_{ads}(O_2)$) at Ru/CZO, Pd/CZO and RuPd/CZO catalysts are −1.90, −0.79, and −2.13 eV, respectively. Thirdly, the O-O bond of the adsorbed O_2 molecule is dissociated to produce active atoms (O^*), which combine with the adsorbed NO species forming surface intermediate NO_2^* species. The third step in the NO oxidation is generally regarded as the rate-determining step, and the energy barriers (E_a) of those processes are as follows: Ru/CZO (1.31 eV), Pd/CZO (1.62 eV) and RuPd/CZO (0.93 eV), indicating that the NO molecules are most prone to react at the binary RuPd site to form NO_2. Fourthly, the NO_2 species is desorbed from the catalyst surface. The NO_2 desorption energy ($E_{des}(NO_2)$) of RuPd/CZO (2.09 eV) is lower than that of Ru/CZO (2.36 eV) and Pd/CZO (2.21 eV), suggesting that NO_2 is more easily desorbed from the binary RuPd site compared to the single Ru and Pd sites. Fifthly, the free NO molecules are adsorbed onto the Ru or Pd sites and continue to react with O^* adsorbed on the catalyst to form ONO^* species. Finally, NO_2^* species is desorbed from the catalyst surface, which fulfills the cyclic process of NO oxidation on the surface of catalysts. The calculated values of E_a and $E_{des}(NO_2)$ for NO_2 species illustrate that the single Ru site is more efficient in NO oxidation compared to the single Pd site, and NO_2 tend to be generated at binary RuPd site relative to the single Ru site. The generated NO_2 can migrate to the soot surface with the gas flow through hierarchical porous structure, and oxidize soot to CO_2 ($NO + 1/2O_2 \rightarrow NO_2$ and $NO_2 + soot \rightarrow CO_2$).

The first C-H dissociation of CH_4 molecule over the Ru/CZO, Pd/CZO and RuPd/CZO catalysts ($CH_4 \rightarrow CH_3 + H$), as a rate-determining step in CH_4 oxidation, are used to study the CH_4 reactivity on different active sites (Figs. 5b and S25)[45,46]. The energy barriers of the first C-H dissociation at single Ru, single Pd and binary RuPd sites are 1.91, 1.63, and 1.03 eV, respectively. The lower energy barriers of first C-H bond dissociation indicate that the reactivity of CH_4 molecule at single Pd site is significantly superior than single Ru site, and the binary RuPd site exhibits superior reactivity of CH_4 molecule compared to the single Pd site. The full energy diagram for CH_4 oxidation to CO_2 and H_2O is present to study the effect of O_2 on CH_4 dehydrogenation (Fig. S26). Firstly, a gaseous O_2 is adsorbed at the interface between noble metal sites (Ru, Pd, and RuPd) and Ce-Zr support via O-Ce and O-M (M = Ru or Pd) bonds forming surface adsorbed O_2^*. The O_2 adsorption energies ($E_{ads}(O_2)$) at Ru/CZO, Pd/CZO and RuPd/CZO catalysts are −1.73, −1.26, and −1.89 eV respectively, indicating that the binary RuPd site exhibits the strongest adsorption capacity of O_2 relative to single Ru and Pd sites. Then, the first C-H bond of the adsorbed CH_4 molecule is broken forming the $^*O$-H, active atoms (O^*) and adsorbed $^*CH_3$ species in the presence of O_2, and the formation of the $^*OH$ also leads to cleavage of the O_2^* molecule. As shown in Fig. 5c, the first C-H bond dissociation generates a more stable final state with lower energy in the presence of O_2 ($CH_4 + O_2 \rightarrow CH_3 + O + OH$), which suggests that O_2^* can promote the first C-H bond dissociation. The energy barriers of the first C-H bond dissociation with O_2-assisted regime at single Ru, single Pd and binary RuPd sites are 2.30, 1.81, and 1.24 eV, respectively, indicating that binary RuPd site exhibits superior reactivity of CH_4 molecule compared to the single Ru and Pd sites. Subsequently, the adsorbed $^*CH_3$ species migrates to the interface and combines with O^* to form methoxy ($^*OCH_3$) species for subsequent oxidation reactions, which require the lower absorption energy for RuPd/CZO (0.17 eV) relative to Ru/CZO (0.52 eV) and Pd/CZO (0.42 eV). It implies that $^*OCH_3$ species, as the key intermediate species, is most prone to be generated on RuPd/CZO. The second H atom separates from $^*OCH_3$ and

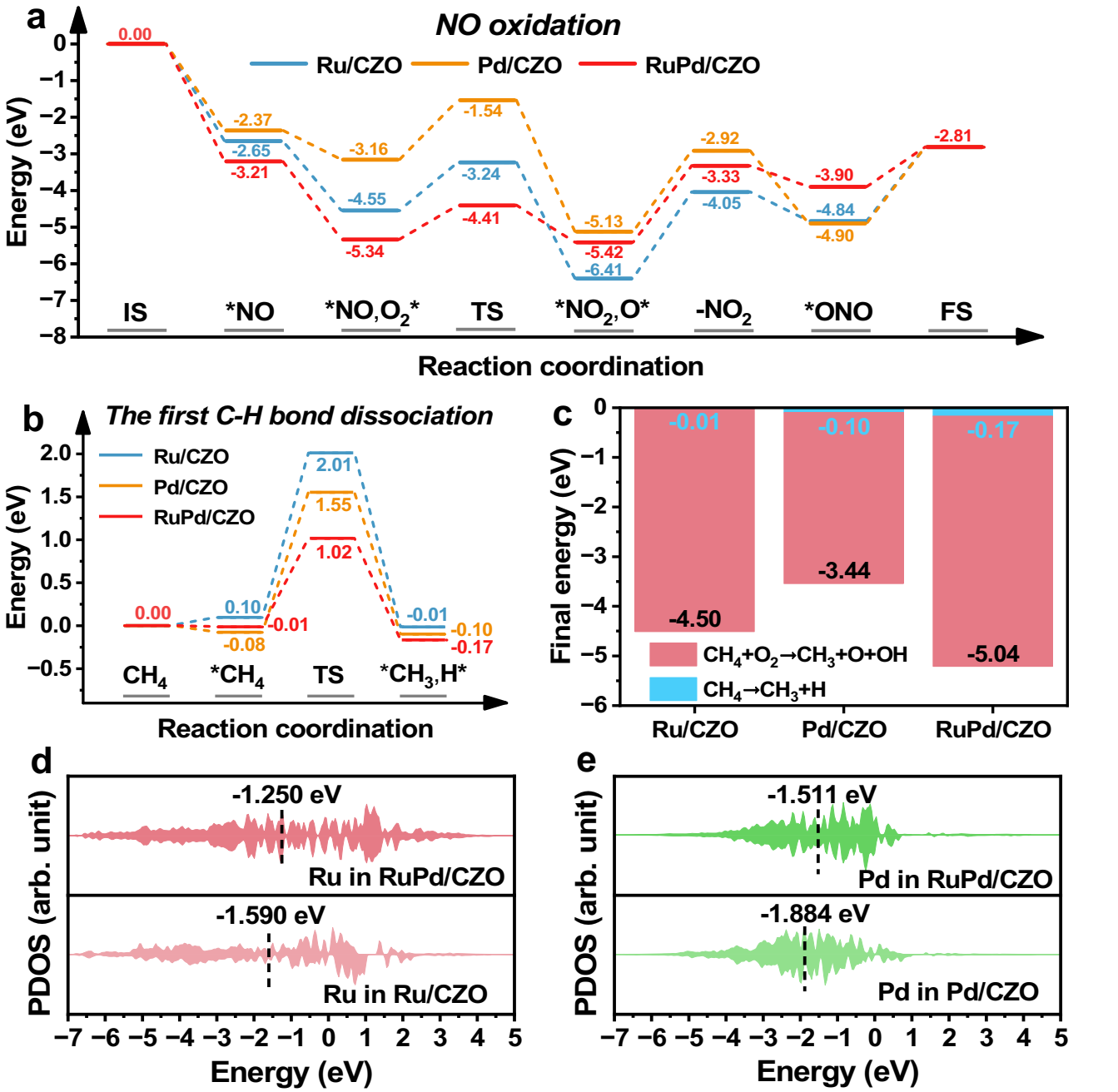

Fig. 5 | DFT calculations of NO and CH_4 oxidation on Ru/CZO, Pd/CZO and RuPd/CZO catalysts. Energy change diagram for catalytic NO oxidation to NO_2 (**a**) and the first C-H bond dissociation of a CH_4 molecule (**b**). Final energy of the first C-H bond dissociation in the presence/absence of O_2 (**c**). The PDOS of Ru-*4d* orbital in Ru/CZO and RuPd/CZO (**d**). The PDOS of Pd-*4d* orbital in Pd/CZO and RuPd/CZO (**e**).

combines with $^*OH$ forming adsorbed H_2O^*, which releases energy of 1.03, 1.27 and 1.25 eV on Ru/CZO, Pd/CZO, and RuPd/CZO, respectively. After H_2O^* is desorbed from Ce-based support, the Ce site can continue to adsorb O_2 molecules. The O_2 adsorption energies ($E_{ads}(O_2)$) at Ru/CZO, Pd/CZO and RuPd/CZO catalysts are −1.29, −1.24 and −1.31 eV, respectively. And then, the H atom and $^*OCH$ species, created by the third C-H bond dissociation, combine with the two O^* to form $^*OH$ and formate ($^*COOH$) species respectively, and the releases energy of those processes are as follows: Ru/CZO (0.11 eV), Pd/CZO (2.55 eV) and RuPd/CZO (1.85 eV). The C-H bond dissociation of $^*COOH$ species results in the formation of $^*CO_2$ and H atom, and the generated H atom combines with HO^* to form H_2O^*. Finally, CO_2^* and H_2O^* species are desorbed from the catalyst surface, which fulfills the cyclic process of CH_4 oxidation on the surface of catalysts.

To reveal the origin for catalytic cooperation between Ru and Pd atoms, the projected densities of state (PDOS) for Ru/CZO, Pd/CZO and RuPd/CZO concentrating on d orbitals of Ru and Pd were simulated (Fig. 5d, e). According to the d-band center theory, the d-band centers of Ru (−1.250 eV) and Pd (−1.511 eV) in RuPd/CZO shift toward the Fermi level relative to that of Ru in Ru/CZO (−1.590 eV) and Pd in Pd/CZO (−1.884 eV), indicating that the adsorption of gaseous reactant on RuPd/CZO is stronger than that on Ru/CZO and Pd/CZO[47]. And in Fig. S27, a significant overlap between the Ru−*4d* and Pd-*4d* orbitals of RuPd/CZO catalyst can be observed between −4 and 0 eV, implying that the formation of the Ru-Pd electronic interaction. The

cooperation between Ru-Pd accelerates the rate-determining step of NO oxidation and CH_4 activation, which leads to the excellent catalytic activity of RuPd/CZO catalyst for simultaneous soot and CH_4 oxidation.

Based on the above results, we found that Ru site in the RuPd NPs is responsible for catalyzing NO oxidation to NO_2, while Pd site can activate the C-H bond for boosting CH_4 oxidation to CO_2. The interface site is the key for adsorption-activation of O_2. NO and CH_4 oxidation reactions occur efficiently at the interfacial site. And the catalytic properties at Ru or Pd sites can be enhanced by incorporating each other to form binary Ru-Pd cooperativity sites, which can suppress the competitive oxidation reactions between NO and CH_4. The conclusion of DFT calculations is consistent with the experimental results. The binary Ru-Pd site easily boosts NO oxidation and C-H bond activation, which is beneficial to further promote simultaneous oxidation of soot and CH_4.

Discussion

In summary, we report a multifunctional RuPd/3DOMM-CZO catalyst for engine exhaust aftertreatment of natural gas-diesel dual-fuel engines. The ordered macropore and mesopore structure in novel hierarchical porous catalysts can respectively enhance the mass transfer diffusion of solid and gaseous reactants for boosting simultaneous soot and CH_4 oxidation. And the binary Ru-Pd active components can improve activation efficiency for NO and CH_4 molecules. RuPd/3DOMM-CZO catalyst exhibits excellent catalytic performance and stability during simultaneous oxidation of soot and CH_4 compared with single Ru or Pd catalysts and single porous catalysts, i.e., its T_{50} values of soot and CH_4 oxidation are respectively 357 °C and 334 °C, and its efficiency of simultaneous oxidation is 95% at 393 °C. Based on the results of characterizations and DFT calculations, Ru site in binary Ru-Pd active components is responsible for catalyzing NO oxidation to NO_2, which is a key step of NO_x-assisted soot oxidation mechanism, while Pd site can effectively activate the C–H bond for boosting CH_4 oxidation to CO_2. The catalytic cooperation between Ru and Pd atoms in binary Ru-Pd active components can adjust the competing oxidation reaction and promote the rate-determining step to realize simultaneous oxidation of soot and CH_4. This study would provide a reliable solution for the design of multifunctional catalysts and new insights into the simultaneous oxidation of multiple substances.

Methods

Chemicals

Methyl methacrylate ($C_5H_8O_2$, 99%), potassium persulfate ($K_2S_2O_9$, 99%), Pluronic F127 (average Mn ~5800), ethanol (CH_3CH_2OH, 99.8%), cerium(III) nitrate hexahydrate ($Ce(NO_3)_3{\cdot}6H_2O$, 99%) and zirconyl(IV) chloride octahydrate ($ZrOCl_2{\cdot}8H_2O$, 99%), ruthenium(III) chloride (Ru content 45-55%), palladium(II) nitrate solution (Pd 10 wt% in 10 wt% nitric acid), poly(N-vinyl-2-pyrrolidone) (PVP, 99%), and sodium borohydride ($NaBH_4$, 99%) were purchased from Aladdin Ltd. (Shanghai, China)

Catalyst preparation

Preparation of polymethyl methacrylate microsphere template. The long-range replication Polymethyl methacrylate (PMMA) microspheres were synthesized by modified emulsifier-free emulsion polymerization method with deionized water as solvent. Methyl methacrylate (MMA) as monomer was purified by reduced pressure distillation, and potassium persulfate (KPS) as polymerizer was purified by recrystallization. Deionized water (240 mL) and MMA (120 mL) were poured into a 2000 mL four-necked flask. The mixture was heated to 80 °C by a hot water bath and stayed stable for 20 min. A Teflon stirring paddle attached to the flask was driven by an electric motor after nitrogen was bubbled to deaerate the air completely. In another beaker, 0.3 g KPS was added into the 40 mL deionized water to form a solution and kept in 80 °C by a water bath. After the temperature of flask stayed stable for a while, the KPS solution was added into the flask rapidly. Under the constant stirring rate (380 r min^{-1}) and the protection of nitrogen, the mixture was kept at 80 °C for 90 min. Waiting for the polyreaction reaction finished, the reaction system was cooled to room temperature, and the homogeneous latex with nearly monodispersed PMMA microspheres were obtained by the filtration with filter paper (pore sizes, ~1 μm). The filtered latex was centrifuged at 3000 rpm (1006.2 g) for 600 min to form tightly packed PMMA microspheres. Removing the supernatant liquid, the solid block was dried at 50 °C for 36 h. Finally, long-range replication PMMA template was obtained.

Preparation of hierarchical porous $Ce_{0.3}Zr_{0.7}O_2$ solid solution. The hierarchical porous $Ce_{0.3}Zr_{0.7}O_2$ solid solution was fabricated by the evaporation-induced self-assembly with colloid crystal template (EISA-CCT) method. 1.0 g Pluronic F127 was dissolved in 10.0 mL ethanol under stirring in 40 °C water-bath and the settled solution was marked as solution A. 3 mmol cerium(III) nitrate hexahydrate and 7 mmol zirconyl(IV) chloride octahydrate were dissolved in 10.0 mL ethanol under stirring in 40 °C water-bath, and the settled solution was marked as solution B. Waiting for solution A and B dissolved completely for 2 h, solution B was dropped into solution A dropwise with gentle stirring. After 4 h of continuous thermostatic mixing, the mixture turned into a translucent sol state. Then the sol was mixed with 3.5 g PMMA microsphere template. After being impregnated completely and filtered, the solid-liquid mixture was put into vacuum oven at 50 °C to age for 8 h. The obtained light-yellow solid after the aging process was calcined in the air ambient at a ramp of 2 °C min^{-1} from room temperature to 500 °C and kept for 240 min, then cooled to room temperature. the desired three-dimensional ordered macro-mesoporous cerium-zirconium oxide was obtained, abbreviated as 3DOMM-CZO.

Preparation of 3DOMM-CZO supported binary Ru-Pd components catalyst. The 3DOMM-CZO supported binary Ru-Pd components catalyst was synthesized by the gas bubbling-assisted membrane reduction (GBMR) method. 0.5 g 3DOMM-CZO support was distributed in 200 mL of deionized water with stirring vigorously. The ruthenium(III) chloride and palladium(II) nitrate solutions were mixed thoroughly before being added to the $Ce_{0.3}Zr_{0.7}O_2$ slurry and stirred for 1.5 h after mixing with the slurry. Theoretically, the supporting of Ru-Pd components were 2 wt%. The stabilizer poly (N-vinyl-2-pyrrolidone) (PVP) solution (20 mL, 1.275 mol L^{-1}) was mixed into the hybrid solution and then stirred thoroughly for 0.5 h. At the same time, sodium borohydride ($NaBH_4$) solution (40 mL, 0.5 g L^{-1}) as the reducing agent was slowly injected into the membrane reactor at a rate of 0.6 mL min^{-1} via a constant-flow pump. After the $NaBH_4$ solution was consumed completely, RuPd/3DOMM-CZO catalyst could be obtained just by centrifugation and calcination. The Ru/3DOMM-CZO and Pd/3DOMM-CZO catalysts can be prepared using a similar process.

Characterizations

Powder X-ray diffraction (XRD) patterns were obtained by a diffractometer (Bruker D8 advance) over the 2θ range from 5 to 90 ° with a 5 ° min^{-1} scanning rate using Cu-Kα radiation to obtain the phase structure of all as-prepared catalysts. Scanning electron microscopy (SEM), transmission electron microscope (TEM) images were obtained by Quanta 200 F and FEI Tecnai G2 F20 transmission electron microscope, respectively. ADF/ABF/SE-STEM images and ADF-STEM-EDX (line-scanning profile and mapping) were obtained by Hitachi HF5000, working at an accelerating voltage of 200 kV. The BET surface areas and pore size distribution of catalysts were determined by nitrogen adsorption/desorption in a Micromeritics TriStar-II 3020 instrument at −196°C by N_2 adsorption. The surface element valence state was detected by X-ray photoelectron spectra (*XPS*, XPSPHI−1600 ESCA

spectrometer), calibrated using a C *1s* binding energy of 284.8 eV. Ce L_3-edge X-ray absorption fine structure (XAFS) spectra were measured at the XRD station of beamline 4B9A of Beijing Synchrotron Radiation Facility (BSRF) in fluorescence mode. The X-ray absorption near-edge structure (XANES) spectra of soft X-ray for the O K-edge were collected from the XMCD-B beam lines at National Synchrotron Radiation Laboratory (NSRL), Hefei, China, with the total electron yield mode in a vacuum chamber ($<5 \times 10^{-8}$ Pa). Raman spectra of all catalysts were measured on an inVia Reflex-Renishaw spectrometer with an excitation wave-length of 532 nm. In-situ Raman experiments were conducted on the high-resolution Raman spectrometer system. For in-situ Raman measurements, the catalysts were deposited on an in-situ cell with a quartz window. The sample was pretreated in a N_2 gas flow (50 mL min^{-1}) at 300 °C for 30 min. Then the reaction atmosphere switched to 5 vol% O_2 balanced with N_2 (50 mL min^{-1}) and the temperature is maintained at 300 °C for 20 min. Finally, the gas feed was switched to a 0.1 vol% NO and 0.1 vol% CH_4 balanced with N_2 (50 mL min^{-1}) at 300 °C for 20 min. The spectra were recorded at 10-min intervals. The temperature programmed reduction of hydrogen (H_2-TPR) was carried out on an Automatic Chemisorption Analyzer (BSD-C200, BSD Instrument). The catalysts were pretreated with N_2 at 350 °C for 30 min before test. After cooling to room temperature, H_2-TPR was conducted with flowed the gaseous contained H_2 (7 vol%) balanced with N_2 (30 mL min^{-1}). And the temperature range of the H_2-TPR is 50 to 900 °C with a ramp rate of 10 °C min^{-1}. The temperature-programmed oxidation of NO (NO-TPO) was carried out on a fixed-bed tubular quartz reactor, and the products can be detected by online FT-IR. The catalysts were pretreated with N_2 at 100 °C for 30 min before test. After cooling to room temperature, NO-TPO was conducted with flowed the gaseous contained O_2 (5 vol%) and NO (0.1 vol%) balanced with N_2 (50 mL min^{-1}). And the temperature range of the NO-TPO reaction is 50 to 500 °C with a ramp rate of 2 °C min^{-1}. The temperature-programmed surface reaction of methane (CH_4-TPSR) was carried out on the MS (Hidden, DECRA) to obtain CH_4, CO_2, H_2O, and CO signals. The catalysts were pretreated with Ar at 150 °C for 30 min before test. Then, catalysts were treated with O_2 (5 vol%) balanced with Ar (50 mL min^{-1}) at 400 °C for 30 min. After cooling to room temperature, the excess O_2 was blown off with Ar. Finally, CH_4-TPSR was conducted with flowed the gaseous contained CH_4 (4 vol%) balanced with Ar (50 mL min^{-1}). And the temperature range of the CH_4-TPSR is 50 to 700 °C with a ramp rate of 10 °C min^{-1}. In-situ diffuse reflectance infrared Fourier transforms spectra (in-situ DRIFTS) were carried on a Bruker FT-IR spectrometer (TENSOR II) equipped with a liquid nitrogen-cooling mercury-cadmium-telluride (MCT) detector. The catalyst was added into high-temperature IR cell with ZnSe window, and heated in N_2 flow at 200 °C for 30 min to remove adsorbed H_2O and other materials. After cooling down to 50 °C with N_2 atmosphere, the background spectrum was recorded. Finally, the gas to be measured were fed into cell at a flow rate of 50 mL min^{-1}. IR spectra of NO oxidation were recorded in a flow of 0.1 vol% NO/5 vol% O_2/N_2 balance (50 mL min^{-1}) under heating from 50 to 400 °C; IR spectra of CH_4 oxidation were recorded in a flow of 0.1 vol% CH_4/5 vol% O_2/N_2 balance (50 mL min^{-1}) under heating from 50 to 400 °C; IR spectra of simultaneous NO and CH_4 oxidation were recorded in a flow of 0.1 vol%NO/0.1 vol% CH_4/5 vol% O_2/N_2 balance (50 mL min^{-1}) under heating from 50 to 400 °C.

Catalytic activity and kinetic tests

The simultaneous oxidation catalytic activity and selectivity are evaluated via temperature-programmed oxidation (TPO) reaction with Printex-U modeled soot particles (~25 nm in diameter) and CH_4 dilution gas. The TPO reaction ranges from 150 to 700 °C at a ramping rate of 2 °C min^{-1}. Mixing catalyst (100 mg) and soot particles (5 mg) until loose contact can simulate realistic conditions for catalytic oxidation of soot. The gaseous reactants are flowed at a rate of 50 mL min^{-1} and consisted of O_2 (5 vol%), NO (0.1 vol%) and CH_4 (0.1 vol%) balanced with N_2. The gaseous products after the oxidation reaction occurred are injected into an online gas chromatograph (GC 9890B, Shanghai) equipped with the FID detector via an autosampler for analysis at 5 min intervals. The signals of CO and CO_2 can be detected on the online gas chromatograph at approximately 0.6 and 3.4 min, respectively. As the temperature increases, soot and CH_4 can be oxidized, and thus we are able to obtain temperature-product concentration curves. As the temperature rises with reaction time, soot becomes oxidized fully, and CH_4 can also be fully oxidized at high temperatures. The signal of the CO_2 and CO product stops changing, indicating that the soot was fully oxidized and the signal of CO_2 and CO was generated exclusively by oxidation of CH_4. Catalytic activity is assessed through the T_{10}, T_{50}, and T_{90} values, defined as temperatures at 10%, 50%, and 90% conversion of CH_4 and soot, respectively.

The S_{CO2} is selectivity of CO_2 for simultaneous soot and CH_4 oxidation, which can be calculated by the ratio of CO_2 concentration to the sum of CO and CO_2 concentration according to the Eq. (1):

$$S_{CO2}(\%) = \frac{[CO_2]_{out}}{[CO]_{out} + [CO_2]_{out}} \times 100\% \quad (1)$$

Here, the $[CO_2]_{out}$ and $[CO]_{out}$ represent the outlet CO_2 and CO concentration, respectively.

The CH_4 conversion (X_{CH4}) is calculated from the changed CH_4 concentration according to the Eq. (2):

$$X_{CH4}(\%) = \frac{[CH_4]_{in} - [CH_4]_{out}}{[CH_4]_{in}} \times 100\% \quad (2)$$

The $[CH_4]_{in}$ is the initial concentration of CH_4 in the inlet gas (0.1 vol%). The $[CH_4]_{out}$ is the concentration of unoxidized CH_4 in the outlet gas, which is detected by online gas chromatograph directly.

The soot conversion (X_{soot}) was evaluated from the changed concentration of CO_2 + CO according to the Eq. (3):

$$X_{soot}(\%) = \frac{[CO_2 + CO]_{soot}}{[CO_2 + CO]_{soot,\,total}} \times 100\% \quad (3)$$

The $[CO_2 + CO]_{soot}$ is the concentration of CO_2 + CO generated from soot oxidation at a certain temperature, which is calculated from the CO_2, CO and CH_4 concentrations directly detected by the online gas chromatograph. The $[CO_2 + CO]_{soot}$ is equal to the concentration of CO_2 + CO generated from simultaneous oxidation minus the concentration of oxidized CH_4, i.e., $[CO_2 + CO]_{soot} = [CO_2]_{out} + [CO]_{out} - ([CH_4]_{in} - [CH_4]_{out})$. The $[CO_2 + CO]_{soot,total}$ is the total concentration of CO_2 + CO generated by complete soot oxidation, which is obtained by integrating $[CO_2 + CO]_{soot}$.

The apparent activation energy of soot oxidation was measured by the single heating rate method (Coats-Redfern integral method) according to the Eq. (4):

$$\beta \frac{d\alpha}{dT} = k(T)f(\alpha) \rightarrow \beta \frac{d\alpha}{dT} = A \times \exp\left(-\frac{E_a}{RT}\right) f(\alpha) \quad (4)$$

Where β is the heating rate (K min^{-1}), α is the soot conversion rate (α < 15 %), T is the reaction temperature (K), k is the reaction rate constant, f(α) is the kinetic expression for the reaction model, $f(\alpha)=(1-\alpha)^n$, where n is the number of reaction stages. A is the pre-finger factor (s^{-1}), E_a is the apparent activation energy (kJ mol^{-1}), R is the ideal gas constant. Previous studies have shown that the reaction of soot with NO_2 is a one-stage reaction, i.e., $n = 1$. The Eq. (5) can be obtained:

$$\ln\left[-\frac{\ln(1-\alpha)}{T^2}\right] = \ln\left[\frac{AR}{\beta E_a}\left(1 - \frac{2RT}{E_a}\right)\right] - \frac{E_a}{RT} \quad (5)$$

In most cases, $\frac{2RT}{E_a}$ much smaller than 1, and $\ln\left[\frac{AR}{\beta E_a}\left(1-\frac{2RT}{E_a}\right)\right]$ can be regarded as a constant. Then, the apparent activation energy is estimated by plotting $\ln[-\frac{\ln(1-\alpha)}{T^2}]$ vs 1/RT.

When the conversion of CH_4 is <15 %, a dependence of the CH_4 reaction rate (r_{CH4}) on the products of CO_2 and H_2O could be ignored; therefore, the empirical kinetic expression of the reaction rate of CH_4 oxidation can be described by Eq. (6):

$$r_{CH4} = \frac{[CH_4] \times X_{CH4} \times F}{m_{catalyst}} \quad (6)$$

where $[CH_4]$ is the CH_4 concentration in the feed gas, X_{CH4} is the CH_4 conversion, F represents the total flow rate (mL min^{-1}) and $m_{catalyst}$ is the catalyst mass (g). The apparent activation energy of CH_4 oxidation is measured according to Eq. (7):

$$\ln r_{CH4} = -\frac{E_a}{RT} + \ln A + a\ln[CH_4] + b\ln[O_2] \quad (7)$$

When the CH_4 conversion is very low (<15%), both CH_4 and O_2 conversions are approximately constant, and the correlation between $\ln r_{CH4}$ and 1/RT is close to linear:

$$\ln r_{CH4} = -\frac{E_a}{RT} + \ln A \quad (8)$$

Where E_a is the apparent activation energy (kJ mol^{-1}), r_{CH4} is the reaction rate (mol g^{-1} s^{-1}) and A is pre-finger factor (s^{-1}). Then, the apparent activation energy is estimated by plotting $\ln r_{CH4}$ vs 1/RT.

Density functional theory (DFT) calculations

DFT calculations were conducted using the VASP package code[48]. The exchange-correlation energy function was described using the Pardew–Burke–Ernzerhof (PBE) generalized gradient approximation (GGA)[49]. The kinetic cutoff energy is 400 eV for the plane-wave basis set, and the k point was set to the γ point in the Brillouin zone. Ce-Zr oxide models were obtained by substitution of Ce atoms for Zr atoms at eight vertices of the ZrO_2 cubic cell[50]. All calculations for Ce atoms of Ce-Zr oxide models were performed by the DFT + U method. The value of U_{eff} was set to 4.5 eV for Ce *4f*[51]. Ce-Zr oxide supercells (2 × 2) were built, with (111) surfaces exposed. The bottom three atomic layers were fixed during all calculations. The thinness of the vacuum layer for all the models was set as 17 Å. Ce-Zr oxide slab had been established and the 10-atom active sites had been inserted into our slab models. The adsorption and desorption energy were calculated by the equations:

$$E_{ads} = E_{MS} - E_S - E_M \quad (9)$$

$$E_{des} = ES + E_M - E_{MS} \quad (10)$$

Where E_{ads} is the adsorption energy, E_{des} is the desorption energy, E_{MS} is the total energy of a surface slab with the adsorbate, and E_S is the energy of pure substrate. E_M represents the energy of an adsorbate molecule.

The climbing image-nudged elastic band (CI-NEB) code was used to identify the reaction coordinates from initial state (IS) to final state (FS)[52], which located the transition state (TS). The activation energy (E_a) was determined with the following equation:

$$E_a = E_{TS} - E_{IS} \quad (11)$$

Where E_{IS} and E_{TS} represent the energy of IS and TS, respectively.

Data availability

The data that support the findings of this study are included in the published article (and its Supplementary Information). Source data are provided with this manuscript and is available from the corresponding author upon request. Source data are provided with this paper.

References

1. Karim, G. A. A review of combustion processes in the dual fuel engine—The gas diesel engine. *Prog. Energy Combust.* **6**, 277–285 (1980).
2. Cesar de Lima Nogueira, S. et al. Prediction of the NO_x and CO_2 emissions from an experimental dual fuel engine using optimized random forest combined with feature engineering. *Energy* **280**, 128066 (2023).
3. Janssens, T. V. W. & Vennestrøm, P. N. R. A molecular dance to cleaner air. *Science* **357**, 866–867 (2017).
4. Mei, X. et al. Decreasing the catalytic ignition temperature of diesel soot using electrified conductive oxide catalysts. *Nat. Catal.* **4**, 1002–1011 (2021).
5. Wang, W. et al. Mixed-phase oxide catalyst based on Mn-mullite (Sm, Gd) Mn_2O_5 for NO oxidation in diesel exhaust. *Science* **337**, 832–835 (2012).
6. McCarty, J. G. Durable catalysts for cleaner air. *Nature* **403**, 35–36 (2000).
7. Farrauto, R. J. Low-temperature oxidation of methane. *Science* **337**, 659–660 (2012).
8. He, C. et al. Recent advances in the catalytic oxidation of volatile organic compounds: a review based on pollutant sorts and sources. *Chem. Rev.* **119**, 4471–4568 (2019).
9. Wei, Y. et al. Highly active catalysts of gold nanoparticles supported on three-dimensionally ordered macroporous $LaFeO_3$ for soot oxidation. *Angew. Chem. Int. Ed.* **50**, 2326–2329 (2011).
10. Mortensen, M. & Laursen, S. Catalytic site seeing. *Nat. Chem.* **14**, 483–485 (2022).
11. Guo, Y. et al. Photo-thermo semi-hydrogenation of acetylene on Pd1/TiO2 single-atom catalyst. *Nat. Commun.* **13**, 2648 (2022).
12. Tang, Y. et al. Synergy of single-atom Ni1 and Ru1 sites on CeO_2 for dry reforming of CH4. *J. Am. Chem. Soc.* **141**, 7283–7293 (2019).
13. Zhang, P. et al. Boosting catalytic purification of soot particles over double Perovskite-type $La_{2-x}K_xNiCoO_6$ catalysts with an ordered macroporous structure. *Environ. Sci. Technol.* **55**, 11245–11254 (2021).
14. Xiong, J. et al. Synergetic effect of K sites and Pt nanoclusters in an ordered hierarchical porous Pt-$KMnO_x$/$Ce_{0.25}Zr_{0.75}O_2$ catalyst for boosting soot oxidation. *ACS Catal.* **10**, 7123–7135 (2020).
15. Li, Y. et al. A single site ruthenium catalyst for robust soot oxidation without platinum or palladium. *Nat. Commun.* **14**, 7149 (2023).
16. Zhao, M. & Xia, Y. Crystal-phase and surface-structure engineering of ruthenium nanocrystals. *Nat. Rev. Mater.* **5**, 440–459 (2020).
17. Enache, D. I. et al. Solvent-free oxidation of primary alcohols to aldehydes using Au-Pd/TiO_2 catalysts. *Science* **311**, 362–365 (2006).
18. Mori, K., Sano, T., Kobayashi, H. & Yamashita, H. Surface engineering of a supported PdAg catalyst for hydrogenation of CO_2 to formic acid: elucidating the active Pd atoms in alloy nanoparticles. *J. Am. Chem. Soc.* **140**, 8902–8909 (2018).
19. Jiang, D. et al. Dynamic and reversible transformations of subnanometre-sized palladium on ceria for efficient methane removal. *Nat. Catal.* **6**, 618–627 (2023).
20. Willis, J. J. et al. Systematic identification of promoters for methane oxidation catalysts using size- and composition-controlled Pd-

based bimetallic nanocrystals. *J. Am. Chem. Soc.* **139**, 11989–11997 (2017).
21. Wei, Y. et al. Fabrication of inverse opal TiO_2-supported Au@CdS core–shell nanoparticles for efficient photocatalytic CO_2 conversion. *Appl. Catal. B* **179**, 422–432 (2015).
22. Wei, Y. et al. Preparation and characterization of $Co_{0.2}/Ce_{1-x}Zr_xO_2$ catalysts and their catalytic activity for soot combustion. *Chin. J. Catal.* **31**, 283–288 (2010).
23. Wang, C. et al. Structural regulation of Au-Pt bimetallic aerogels for catalyzing the glucose cascade reaction. *Adv. Mater.* **36**, 2405200 (2024).
24. Tang, M. et al. RuPd alloy nanoparticles supported on N-doped carbon as an efficient and stable catalyst for benzoic acid hydrogenation. *ACS Catal.* **5**, 3100–3107 (2015).
25. Jung, Y. & Bae, C. Immaturity of soot particles in exhaust gas for low temperature diesel combustion in a direct injection compression ignition engine. *Fuel* **161**, 312–322 (2015).
26. Andana, T. et al. CuO nanoparticles supported by ceria for NO_x-assisted soot oxidation: insight into catalytic activity and sintering. *Appl. Catal. B* **216**, 41–58 (2017).
27. Guo, S.-N., Dong, Y.-J., Qiao, M., Wang, D. & Wang, J.-X. Variable valence Ce-based $Cs_2CeAgBr_6$ perovskite nanocrystals for highly selective photoconversion of CO_2 to CH_4. *Small* **21**, 2408765 (2025).
28. Liu, Y., Sheng, W. & Wu, Z. Synchrotron radiation and its applications progress in inorganic materials. *J. Inorg. Mater.* **36**, 901–918 (2021).
29. Cheng, W. et al. Recent advances in battery characterization using in situ XAFS, SAXS, XRD, and their combining techniques: from single scale to multiscale structure detection. *Exploration* **4**, 20230056 (2024).
30. Zhao, S. et al. Spontaneous formation of asymmetric oxygen vacancies in transition-metal-doped CeO_2 nanorods with improved activity for carbonyl sulfide hydrolysis. *ACS Catal.* **10**, 11739–11750 (2020).
31. Barreau, M. et al. Ionic Nickel embedded in ceria with high specific CO_2 methanation activity. *Angew. Chem. Int. Ed.* **62**, e202302087 (2023).
32. Wilson, H. H. et al. Synthesis and characterization of a bridging cerium (IV) nitride complex. *J. Am. Chem. Soc.* **145**, 781–786 (2023).
33. Xiong, J. et al. Highly reactive peroxide species promoted soot oxidation over an ordered macroporous $Ce_{0.8}Zr_{0.2}O_2$ integrated catalyzed diesel particulate filter. *Environ. Sci. Technol.* **58**, 8096–8108 (2024).
34. Feng, X. et al. Unraveling the principles of lattice disorder degree of $Bi_2B_2O_7$ (B = Sn, Ti, Zr) compounds on activating gas phase O_2 for soot combustion. *ACS Catal.* **11**, 12112–12122 (2021).
35. Li, Y. et al. Enhancing catalytic removal of autoexhaust soot particles via the modulation of interfacial oxygen vacancies in Cu/CeO_2 catalysts. *Environ. Sci. Technol.* **59**, 2327–2338 (2025).
36. Chen, J., Liu, X. & Zhang, F. Composition regulation of bimetallic RuPd catalysts supported on porous alumina spheres for selective hydrogenation. *Chem. Eng. J.* **259**, 43–52 (2015).
37. He, Y. et al. In situ identification of reaction intermediates and mechanistic understandings of methane oxidation over hematite: a combined experimental and theoretical study. *J. Am. Chem. Soc.* **142**, 17119–17130 (2020).
38. Tamm, S., Vallim, N., Skoglundh, M. & Olsson, L. The influence of hydrogen on the stability of nitrates during H_2-assisted SCR over Ag/Al_2O_3 catalysts—a DRIFT study. *J. Catal.* **307**, 153–161 (2013).
39. Hu, H. et al. Mechanistic aspects of deNOx processing over TiO_2 supported Co–Mn oxide catalysts: structure–activity relationships and in situ DRIFTs analysis. *ACS Catal.* **5**, 6069–6077 (2015).
40. Wang, L., Cheng, X., Wang, Z., Ma, C. & Qin, Y. Investigation on Fe-Co binary metal oxides supported on activated semi-coke for NO reduction by CO. *Appl. Catal. B* **201**, 636–651 (2017).
41. Yao, X. et al. A comparative study of different doped metal cations on the reduction, adsorption and activity of $CuO/Ce_{0.67}M_{0.33}O_2$ ($M=Zr^{4+}$, Sn^{4+}, Ti^{4+}) catalysts for NO+CO reaction. *Appl. Catal. B* **130-131**, 293–304 (2013).
42. Zhang, S. et al. Catalysis on singly dispersed Rh atoms anchored on an inert support. *ACS Catal.* **8**, 110–121 (2018).
43. Artsiusheuski, M. A., Verel, R., van Bokhoven, J. A. & Sushkevich, V. L. Methane transformation over copper-exchanged zeolites: from partial oxidation to C–C coupling and formation of hydrocarbons. *ACS Catal.* **11**, 12543–12556 (2021).
44. Li, Q. et al. Metal–support interactions within a dual-site Pd/YMn_2O_5 catalyst during CH_4 combustion. *ACS Catal.* **12**, 4430–4439 (2022).
45. Chin, Y.-H., Buda, C., Neurock, M. & Iglesia, E. Consequences of metal–oxide interconversion for C–H bond activation during CH_4 reactions on Pd catalysts. *J. Am. Chem. Soc.* **135**, 15425–15442 (2013).
46. Tao, F. F. et al. Understanding complete oxidation of methane on spinel oxides at a molecular level. *Nat. Commun.* **6**, 7798 (2015).
47. Tao, L. et al. Precise synthetic control of exclusive ligand effect boosts oxygen reduction catalysis. *Nat. Commun.* **14**, 6893 (2023).
48. Kresse, G. & Furthmüller, J. Efficient iterative schemes for ab initio total-energy calculations using a plane-wave basis set. *Phys. Rev. B* **54**, 11169–11186 (1996).
49. Kresse, G. & Furthmüller, J. Efficiency of ab-initio total energy calculations for metals and semiconductors using a plane-wave basis set. *Comp. Mater. Sci.* **6**, 15–50 (1996).
50. Yashima, M. Crystal structures of the tetragonal ceria-zirconia solid solutions $Ce_xZr_{1-x}O_2$ through first principles calculations ($0 \le x \le 1$). *J. Phys. Chem. C.* **113**, 12658–12662 (2009).
51. Tan, R. et al. Liberating C–H bond activation: achieving 56% quantum efficiency in photocatalytic cyclohexane dehydrogenation. *J. Am. Chem. Soc.* **146**, 14149–14156 (2024).
52. Henkelman, G., Uberuaga, B. P. & Jónsson, H. A climbing image nudged elastic band method for finding saddle points and minimum energy paths. *J. Chem. Phys.* **113**, 9901–9904 (2000).

Acknowledgements

This work was financially supported by National Key Research and Development Program of China (2022YFB3504100), National Natural Science Foundation of China (22208373, 22376217, 12305372), Key Laboratory of Jiangxi Province for Persistent Pollutants Prevention Control and Resource Reuse (2023SSY02061), and Financial Support by Open Research Fund of Key Laboratory of the Ministry of Education for Advanced Catalysis Materials and Zhejiang Key Laboratory for Reactive Chemistry on Solid Surfaces in Zhejiang Normal University (KLMEACM202303). We thank the 4B9A beamline (https://cstr.cn/31109.02.BSRF.4B9A) of Beijing Synchrotron Radiation Facility (BSRF) for providing technical support and assistance in XAFS data collection.

Author contributions

L.X. and Y.W. conceived, synthesized the catalyst and completed most of the experiments and characterizations, and wrote the paper. T.Q., X.L., and Q.H. completed the electron microscopy test. Y.L., P.Z., and X.Y. helped with the catalytic performance and carried out theoretical calculations and analyses. Y.M., J.X., and Y.L. helped analyze the experiment data. H.G., J.Z., and Z.Z. modified the manuscript. All the authors discussed the results in the manuscript. All authors have approved the final version of the manuscript.

Competing interests

The authors declare no competing interests.

Additional information

Supplementary information The online version contains supplementary material available at https://doi.org/10.1038/s41467-025-63089-8.

Correspondence and requests for materials should be addressed to Xiaolin Yu, Yunpeng Liu or Yuechang Wei.

Peer review information *Nature Communications* thanks Hyung Chul Ham, and Piotr Legutko for their contribution to the peer review of this work. A peer review file is available.